第 48 卷第 1 期　　硅　酸　盐　学　报　　Vol. 48，No. 1
2020 年 1 月　　JOURNAL OF THE CHINESE CERAMIC SOCIETY　　January，2020
http://www.gxyb.cbpt.cnki.net　　**DOI**：10.14062/j.issn.0454-5648.20190283

纳米片层状类石墨氮化碳的制备及其光催化性能

马爱琼[1]，张　电[1]，张由子[2]，高云琴[1]

(1. 西安建筑科技大学材料科学与工程学院，西安 710055；
2. 西北工业大学材料科学与工程学院，西安 710068)

摘　要：以三聚氰胺为原料，采用热缩聚合成法，结合酸、热刻蚀协同改性工艺，制备了二维纳米片层状类石墨氮化碳(g-C_3N_4)。通过 X 射线衍射、扫描电镜、透射电镜、红外光谱、X 射线光电子能谱、Raman 光谱对试样进行了物相组成、显微形貌与分子结构表征。采用 BET 法分析了试样的比表面积，采用紫外–可见漫反射光谱、Mott–Schottky 曲线分析了试样的可见光吸收性能与能带结构。通过可见光降解罗丹明 B 染料与盐酸四环素溶液，评估了试样的可见光催化性能。结果表明：采用热刻蚀改性剥离时，当三聚氰胺与 NH_4Cl 的摩尔比为 5:4 时，所制备的纳米片层状 g-C_3N_4 厚度为 47 nm，比表面积为 22 m^2/g，可见光催化降解性能提高显著，相比未经过改性处理的 g-C_3N_4，其降解效率提高了 3.4 倍；4 h 内对盐酸四环素溶液的降解率达到 83.2%。

关键词：类石墨氮化碳；二维纳米层；可见光；刻蚀；光催化剂
中图分类号：O643　　**文献标志码**：A　　**文章编号**：0454–5648(2020)01–0044–09
网络出版时间：2019–08–30



Preparation and Photocatalytic Properties under Visible Light Irradiation of Graphite-like Carbon Nitride Nanosheets

MA Aiqiong[1], *ZHANG Dian*[1], *ZHANG Youzi*[2], *GAO Yunqin*[1]
(1. College of Materials Science and Engineering, Xi′an University of Architecture &Technology, Xi′an 710055, China;
2. College of Materials Science and Engineering, Northwestern Polytechnical University, Xi′an 710068, China)

Abstract: Graphitic carbon nitride (g-C_3N_4) nanosheet was synthesized by a facile fabrication method. Melamine was treated by a thermal polycondensation process. Pure g-C_3N_4 was treated by acid etching, heat etching and coupling with NH_4Cl. The crystalline structure, morphology, specific surface area, band structure and visible absorption of the material were evaluated by X-ray diffraction, scanning electron microscopy, transmission electron microscopy, Fourier transform infrared spectroscopy analysis, X-ray photoelectron spectroscopy, Raman spectroscopy, specific surface area (BET analysis), ultraviolet visible diffuse reflection spectroscopy and Mott-Schottky curve analysis, respectively. The photocatalytic activity was estimated by the degradation of Rhodamine and tetracycline hydrochloride solution under visible light irradiation. The results show that a clear, ordered, 2D nanosheet g-C_3N_4 structure with a layer thickness of 47 nm is formed, and the maximum specific surface area is a maximum (22 m^2/g) when the mole ratio of melamine to NH_4Cl is 5:4. The photocatalytic performance of bulk g-C_3N_4 is enhanced after treatment. The photocatalytic degradation rate of the sample treated with melamine and NH_4Cl at a ratio of 5:4 is 3.4 times greater than that of untreated g-C_3N_4. The sample degrades 83.2% tetracycline hydrochloride solution for 4 h.

Keywords: graphitic carbon nitride; two-dimensional nanosheet; visible light; etching; photocatalyst

1　Introduction

Due to the rapid depletion of fossil energy and increasing environmental pollution problems, it is highly necessary to develop alternative and renewable energy sources[1–2]. In recent years, semiconductor-based

收稿日期：2019–04–28。　修订日期：2019–05–30。
基金项目：陕西省自然科学基金(2020318029)。
第一作者：马爱琼(1970—)，女，博士，教授。

Received date: 2019–04–28.　**Revised date:** 2019–05–30.
First author: MA Aiqiong (1970–), female, Ph.D., Professor.
E-mail: maaiqiong@xauat.edu.cn

photocatalysis has received great attention. This approach directly converts solar energy to chemical energy or mineralizes organic pollutants, which could be regarded as a long-term solution to address global energy and environmental problems. Nevertheless, the development of efficient, sustainable and environmentally friendly photocatalysts remains a significant challenge[3–4].

Following the work of Fujishima et al. [5–8], titanium dioxide (TiO_2) has become a conventional choice for photocatalysts. However, its wide intrinsic band gap and high recombination rate of photoexcited charge carriers restricts the large-scale and practical exploitation of this material[9–11]. For example, the band gap of TiO_2 is approximately 3.2 eV, indicating that this material can only absorb ultra-violet (UV) light with wavelengths shorter than 387 nm. In addition, the rapid recombination of charge carriers reduces the lifetime of photogenerated electrons and holes and restricts the light-induced redox reaction. Graphitic carbon nitride (g-C_3N_4), which is a 2D π-conjugated polymeric and metal-free semiconductor, has emerged as an attractive candidate since the work of Wang et al. [12–14]. The mild band gap (2.7 eV), excellent chemical stability and unique microstructure endow g-C_3N_4 with outstanding photocatalytic performance. However, the photocatalytic efficiency of bulk g-C_3N_4 is far from meeting the needs of practical application due to the low specific surface area, which does not provide enough reaction sites for the redox reaction. In this paper, an exfoliation method was used in the treatment of g-C_3N_4 to increase the specific surface area and enhance the photocatalytic performance. Using Rhodamine B (RhB) and tetracycline hydrochloride solution as degrading targets, the photocatalytic properties of the prepared 2D nanosheet g-C_3N_4 material were investigated in this work.

2 Experimental

2.1 Synthesis of bulk g-C_3N_4

Bulk g-C_3N_4 was synthesized by thermal polycondensation of melamine (Analytically pure, Sinopharm Chemical Reagent Co., Ltd, China). In detail, melamine powder (5 g) was placed in an alumina crucible with a cover, heated to 550 °C at a heating rate of 2 °C/min and maintained for 3 h. After cooling to room temperature, the resident yellow product was collected, milled into powder, and named CN for further use.

2.2 Treatment of bulk g-C_3N_4

Heat treatment: The CN powder was heated at 550 °C for 3 h, and the obtained powder was named HCN.

NH_4Cl (Analytically pure, Sinopharm Chemical Reagent Co., Ltd, China) addition for synergetic treatment: Different mass ratios from 1:5 to 5:5 of NH_4Cl and melamine were mixed well and placed into a crucible with lid. Then, the samples were heated to 550 °C at a heating rate of 2 °C/min and maintained for 3 h. The prepared samples were named CNN1, CNN2, CNN3, CNN4, and CNN5.

Acid treatment: CN (1 g) was dispersed in a mixture solution of nitric acid (HNO_3, 20 mL) and glacial acetic acid (CH_3COOH, 20 mL) for 2 h at room temperature. Then, the obtained suspension was washed several times with deionized water and dried at 70 °C. After cooling to room temperature, the residual yellow product was collected, milled into powder, and named ACN for further use.

2.3 Photocatalytic experiment

The photocatalytic properties of the samples were evaluated by degrading RhB in an aqueous medium under simulated visible light irradiation. In a typical procedure, as-prepared samples (0.01 g) were dispersed in RhB dye solution (100 mL of 20 mg/L) and stirred in the dark for 30 min to reach adsorption/desorption equilibrium between the catalysts and RhB dye. As a cocatalyst, H_2O_2 was added to the suspension, and then the lamp was turned on (a 500 W xenon lamp with cut-off filter was used to provide visible light with λ>400 nm). The specified dispersions were pipetted at given time intervals and centrifuged to remove the suspended catalysts. Finally, the precipate was collected to measure the residual dye concentration at 510 nm using a ultra-violet visible (UV-vis) spectrophotometer. The degradation efficiency η (%) of the RhB dye solution was evaluated according to Eq. (1):

$$\eta = (c_0 - c_t)/c_0 \times 100\% \quad (1)$$

where c_0 is the initial concentration of the RhB dye solution (mg/L) and c_t is the concentration of the dye at time t (mg/L).

2.4 Characterization

The X-ray diffraction (XRD) patterns of the crystal phase were collected using an Empyrean diffractometer (PANalytical B.V., Holland) with Cu K_α radiation (λ=0.154 18 nm) in the 2θ range of 10°–85°. The microstructures of the samples were characterized by scanning electron microscopy (SEM, FEI Verios 460, Germany, operating at 20 kV) and transmission electron microscopy (TEM, HITACHI H-7650, Japan). The UV-vis diffuse reflectance spectra of the samples were obtained using a UV-vis spectrophotometer (Shimadzu Corporation, UV-2450, Japan). A X-ray photoelectron spectroscopy (XPS, Thermo Fisher ESCALAB Xi, USA) was used to investigate the chemical composition of g-C_3N_4. Raman spectra were collected on a micro-Raman spectrometer (Renishaw inVia, England). Infrared (IR) spectra were measured using a Nicolet Model Nexus 470FT-IR spectrometer (USA) with the pellet technique. Additionally, Motto-Schottky curves were measured using a three-electrode system on a CHI660E B17399 electrochemistry workstation (China).

3 Results and discussion

3.1 Characterization of the 2D g-C_3N_4 nanosheets

The crystal structures of bulk g-C_3N_4 and g-C_3N_4

after treatment were examined by X-ray diffraction (XRD), and the results are depicted in Fig. 1. The layer spacing was calculated according to Bragg's law:

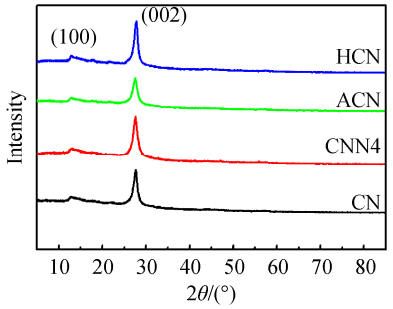
$$2d\sin\theta = n\lambda \quad (2)$$

where d, θ, and λ are the layer spacing (nm), Bragg angle (°) and wavelength (nm), respectively. There are two distinct diffraction peaks at 2θ values of 12.7° and 27.7° that can be indexed as the (100) and (002) diffraction planes for graphite-like carbon nitride materials (JCDPS 87-1526), indicating that the CN exhibits a flake-like structure. The strong peak of CN at 27.7°, corresponding to the (002) plane, is attributed to the interlayer stacking of aromatic segments with a distance of $d_{(002)}$=0.321 nm[15–17]. The weak peak located at 12. 7° is attributed to the in-plane structure packing motif of tri-s-triazine units with an interplanar distance of $d_{(100)}$=0.690 nm[17].

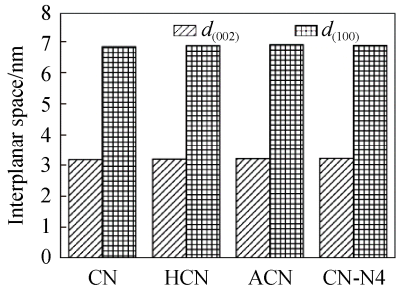
The diffraction angle shifts for the (002) plane and the layer space changes in the (002) and (100) planes with different contents of added NH_4Cl are depicted in Fig. 1c and Fig. 1d. The diffraction angle of the (002) plane changed from 27.46° to 27.7°, according to the XRD results. With changing NH_4Cl content, the layer spacing of the (100) and (002) planes reached the maximum value when the content ratio of NH_4Cl to melamine was 5:4. The addition of NH_4Cl can produce a more complete g-C_3N_4 material by providing a protective atmosphere and preventing the oxidation of melamine during the polycondensation process. The evaporation of NH_4Cl exfoliated the bulk g-C_3N_4 and endowed it with better dispersion. However, excessive addition of NH_4Cl will prevent homogeneous polycondensation so that an incomplete g-C_3N_4 structure will be obtained.

As shown in Fig. 1a and 1b, slight shifts and layer space increases are observed for the (002) and (100) planes, indicating that etching efficiently decreased the interlayer Van der Waals forces and exfoliated the bulk g-C_3N_4. The largest layer spacing of the (100) plane was observed for ACN; the spacing was greater than the tri-s-triazine interplane distance (d=0.672 nm) and that of other treatments, which is due to the damage of the tri-s-triazine structure by acid. Applying coupling treatment with a suitable content of NH_4Cl results in the best exfoliation performance and a more complete structure of g-C_3N_4 than ACN.

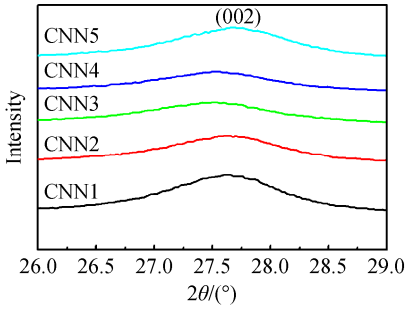
Fig. 2 depicts the IR spectra of g-C_3N_4 samples in the wavenumber range of 500–4 000 cm^{-1}. The broad peak of g-C_3N_4 centered at 3 081 cm^{-1} was assigned to N–H or N=H groups, which were attributed to incomplete condensation[8–19]. Thus, radial hydrogen atoms were bound to the edge of the g-C_3N_4 sheet in the form of CNH_2 and 2CNH bonds. The absorption bands in the range of 1 200–1 600 cm^{-1} were due to the skeletal stretching vibration modes of aromatic heterocycles, including the typical sp^2 C=N stretching signals and in-plane bending vibrations of sp^3 C–N bonds[18]. The vibration peak at 810 cm^{-1} was assigned to the characteristic peak mode of tri-s-triazine[20], in agreement with the XRD results. The IR patterns in Fig. 2a and Fig. 2b indicate that no distinct changes were found for the different g-C_3N_4 samples.



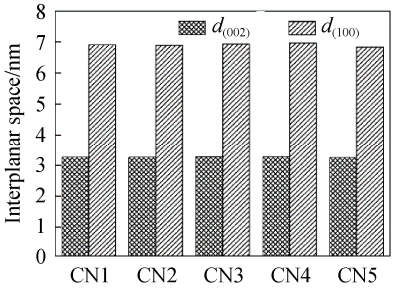
(a) XRD patterns of CN CNN4, HCN, ACN samples



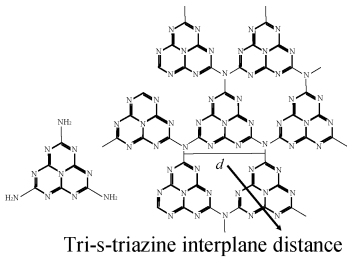
(b) Layer spacing changes of CN, HCN, ACN, CNN4 samples



(c) Diffraction angle changes of the (002) plane of CNN1-CNN5 samples

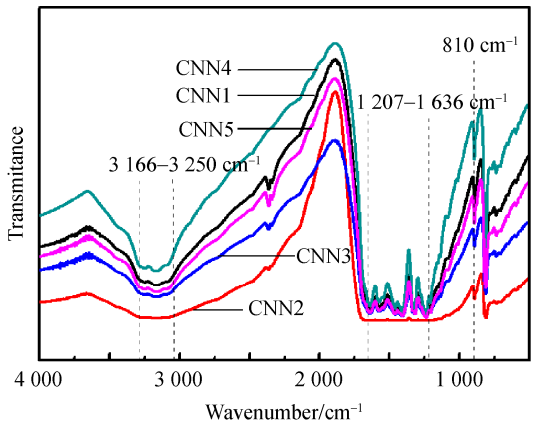


(d) Layer spacing changes of CNN1-CNN5 samples

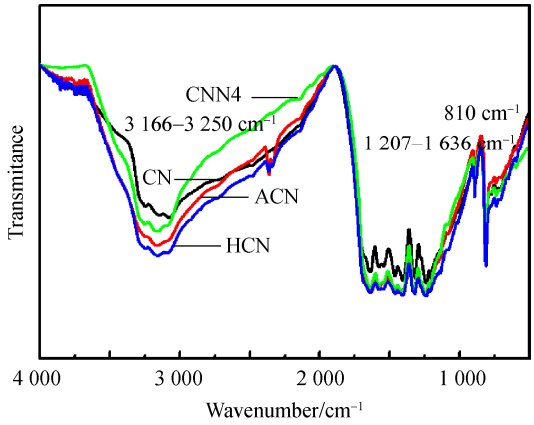


(e) Structure of tri-s-triazine

Fig. 1 XRD patterns of different g-C_3N_4 samples and structure of tri-s-triazine



(a) IR spectra for samples with different treatments



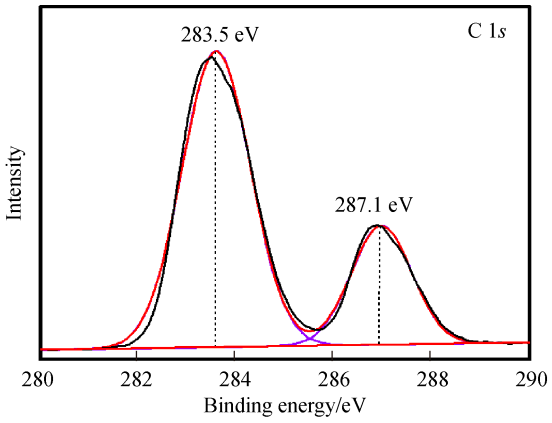
(b) IR spectra for samples with different contents of NH_4Cl addition

Fig. 2　IR spectra of as-prepared samples

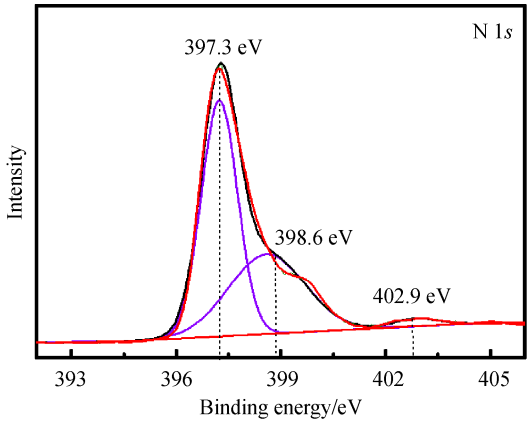
XPS analysis was performed to study the binding energy of different elements under different bonding conditions, as shown in Fig. 3. In Fig. 3a, two peaks are located at 283.5 and 287.1 eV. The peak at 283.5 eV can be caused by a carbon source from the outside environment, unrelated to the samples. The peak at 287.1 eV is attributed to the binding energy of carbon in N=C–N bonds. In Fig. 3b, three peaks are located at 397.3, 398.6 and 402.9 eV. The strongest peak at 397.3 eV is attributed to the binding energy of nitrogen in sp^2 hybrid orbitals (C=N–C bonds). The peak at 398.6 eV is the binding energy of sp^3-bonded N (N–$(C_3N_3)_3$ and HN–$(C_3N_3)_2$). Finally, the binding energy at 402.9 eV is attributed to π-electronic delocalization, which is attributed to CN heterocycles of g-C_3N_4.

Fig. 4 shows the Raman spectrum of the CNN4 sample. The characteristic peaks of the C–N extended network at 707, 767, 1 233 and 1 312 cm^{-1} are consistent with the data in the literature for g-C_3N_4.

Typical SEM images of CN, ACN HCN, and CNN4 are presented in Fig. 5. Fig. 5a shows the large agglomerates of CN. The coexistence of flakes and particles, as shown in Fig. 5b, can result from acid treatment. The acid treatment not only exfoliated the bulk g-C_3N_4 but also destroyed the crystal structure and led to the appearance of this uneven morphology. After heat etching, a clear, ordered, 2D nanosheet g-C_3N_4 material was synthesized, as shown in Fig. 5c, suggesting that heat treatment can efficiently exfoliate bulk g-C_3N_4. Fig. 5d exhibits a well-dispersed 2D nanosheet with a layer thickness of 47 nm prepared by coupling treatment with NH_4Cl. Fig. 6 shows a TEM image of the CNN4 sample. It can be further observed that the g-C_3N_4 material is well dispersed as 2D nanosheets.



(a) C 1*s*



(b) N 1*s*

Fig. 3　XPS spectra of CNN4 sample

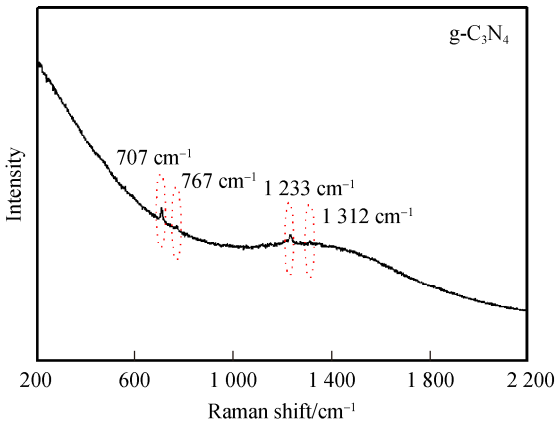
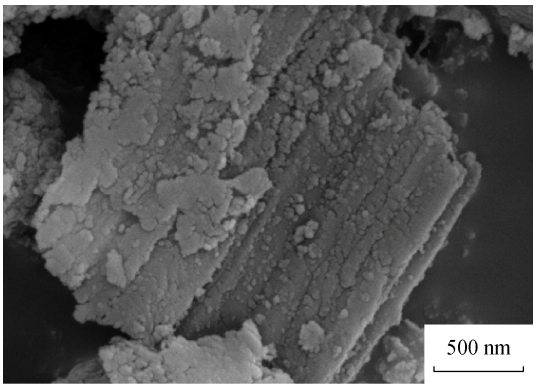
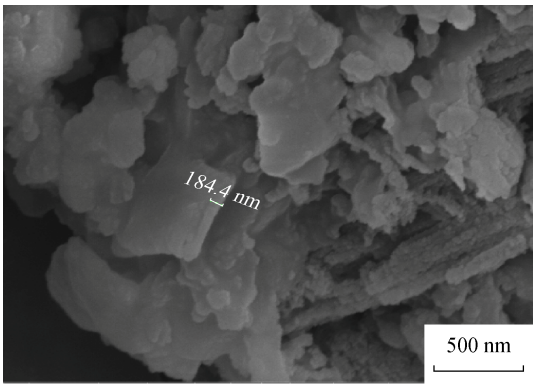


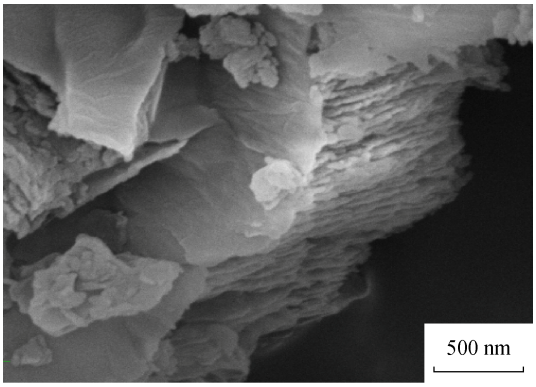
Fig. 4　Raman spectrum of the CNN4 sample



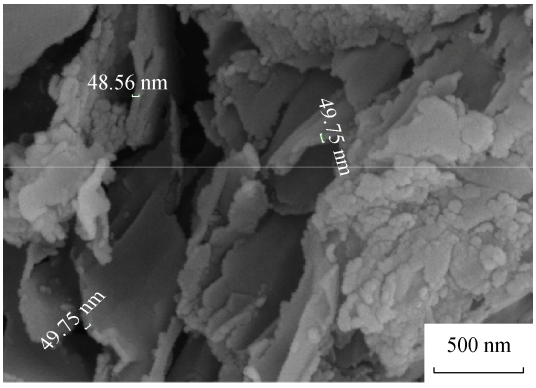
(a) HCN



(b) CAN



(c) CN



(d) CNN4

Fig. 5 SEM images of the samples

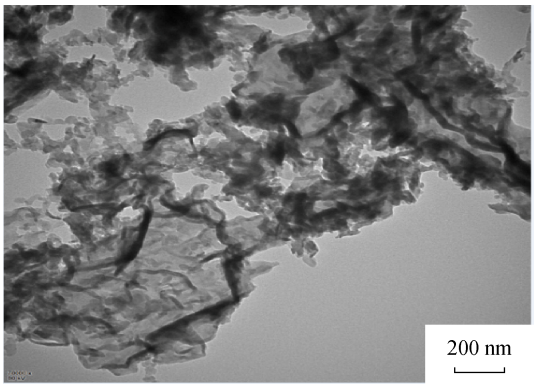


Fig. 6 TEM image of CNN4

The effect of etching on the BET surface area and pore structure of the prepared samples was investigated using absorption–desorption measurements. As shown in Fig.7, the BET surface area of the samples gradually increased with different etching treatments, from 8 m^2/g to 22 m^2/g. Fig. 7a show the nitrogen absorption–desorption isotherms (tested at standard temperature and pressure) and the corresponding pore size distribution curves (inset) for the as-prepared CNN4 samples. According to the Brunauer-Deming-Deming-Teller (BDDT) classification, the majority of physisorption isotherms can be grouped into six types. Typically, CN, CAN, HCN and CNN4 have isotherms of type IV, indicating the presence of mesopores. The shape of the hysteresis loop is that of type H3, suggesting the interlayer stacking of nanosheet-like g-C_3N_4. This result was further confirmed by the corresponding pore size distribution. As shown in the inset of Fig. 7, the samples have mesopores with a size of approximately 4 nm. Consequently, etching treatment can efficiently decrease the interlayer Van der Waals forces, increase the specific surface area and obtain nanosheet g-C_3N_4. The high specific surface area of g-C_3N_4 can supply more active sites and make charge carrier transport easier, leading to an enhancement in the photocatalytic performance.

The light absorption ability of the as-prepared samples was evaluated by UV-vis diffuse reflected absorption spectra. The results are depicted in Fig. 8. The Mott-Schottky (MS) curve of the CNN4 sample is depicted in Fig. 9. The results exhibited good photoabsorption performance in the visible light region. For semiconductors, the band gap of the as-prepared samples can be determined by Tauc's relation[21–23]:

$$\alpha = \frac{c}{h\nu}(h\nu - E_g)^m \tag{3}$$

where α is the absorption coefficient, $h\nu$ is the photon energy, c is the solution concentration, E_g is the optical band gap and m is a constant. The band gap values of CN, HCN, CNN4 and ACN calculated from Eq. (3) were 2.46, 2.46, 2.42 and 2.36 eV, respectively. The valence band (VB) and conduction band (CB) edge potentials of the samples were calculated according to the Mulliken

electronegativity theory using the following equations (Eq.(4)–Eq. (6))[24–26]:

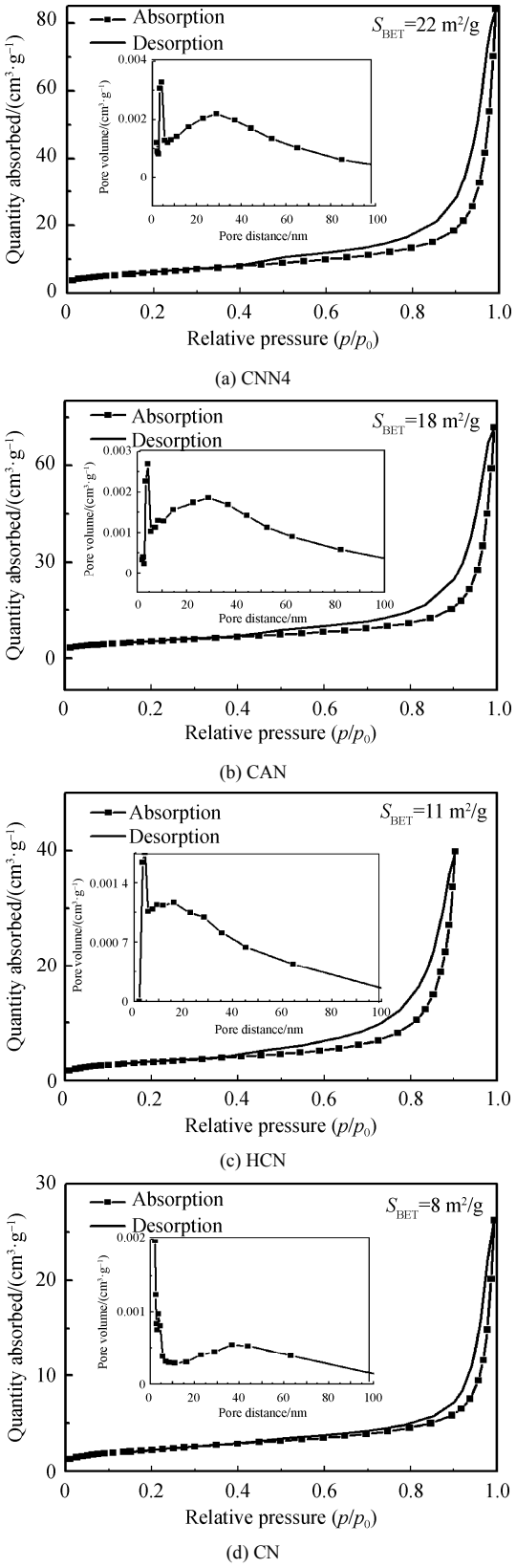


Fig. 7　Nitrogen adsorption–desorption isotherms and corresponding pore size distribution curves (inset) of differently treated samples

$$E_{CB} = X - E_f + 0.5E_g \quad (4)$$

$$E_{VB} = E_g - E_{CB} \quad (5)$$

$$X_{g\text{-}C_3N_4} = \sqrt[7]{X_C^{\,3} X_N^{\,4}} \quad (6)$$

where X and E_g denote the absolute electronegativity and band gap, respectively. E_f is the energy of free electrons on the hydrogen scale (about 4.5 eV). The details of the band structures of the as-prepared samples are shown in Table 1.

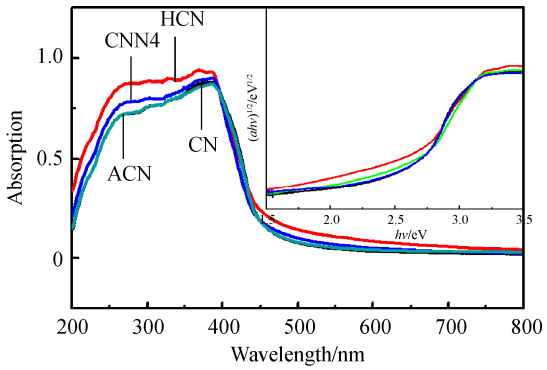


Fig. 8　UV-vis absorption spectra of CN, HCN, CNN4 and CAN

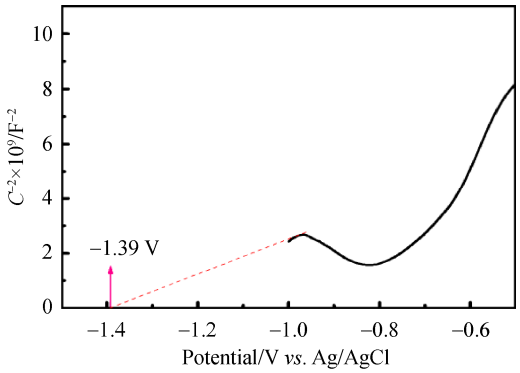


Fig. 9　Mott-Schottky curve of the CNN4 sample

Table 1　Band structures of different samples

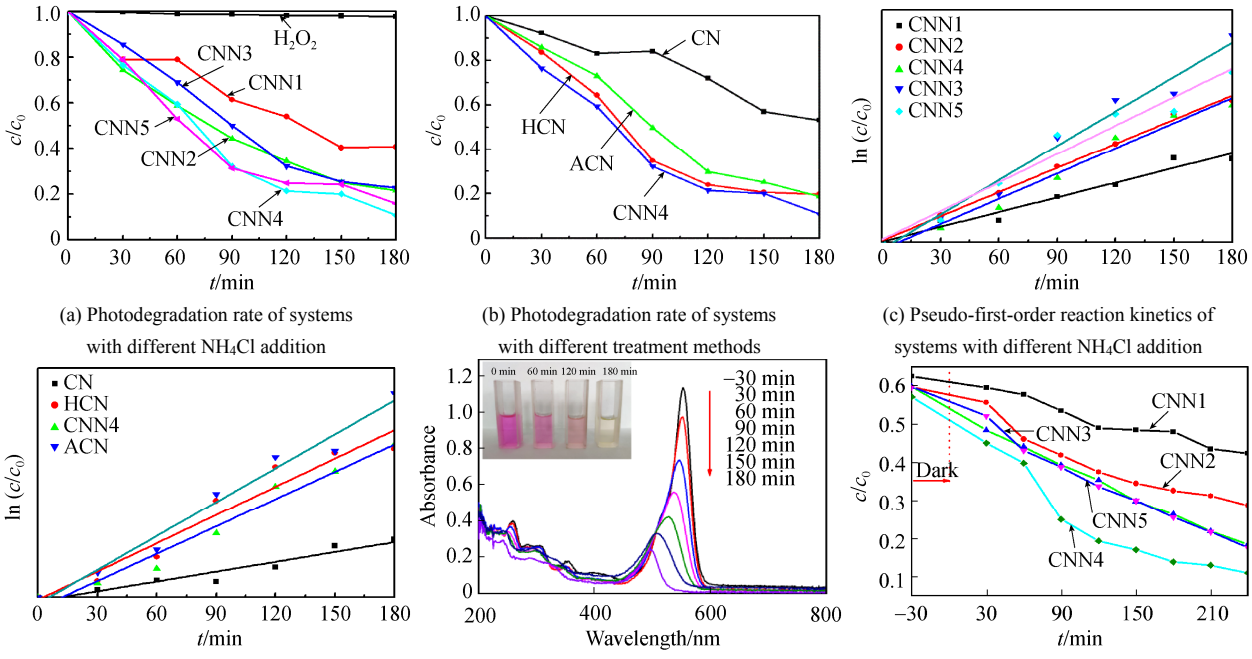
Sample	E_{VB}/eV	E_{CB}/eV	E_g/eV	S_{BET}/(m^2·g^{-1})
CN	1.11	−1.35	2.46	8
ACN	1.16	−1.20	2.36	11
HCN	1.11	−1.35	2.46	18
CNN4	1.15	−1.39	2.42	22

The positive slopes of the linear MS plots reveal the n-type semiconductor characteristics of the as-prepared g-C_3N_4. More importantly, the E_{CB} can be determined from the x-intercept in the MS plot. For the CNN4 sample, the derived E_{CB} potential in aqueous solution is –1.39 V *versus* Ag/AgCl electrode. These data are close to the values in Table 1.

3.2　Photocatalytic performance of the as-prepared samples

The photocatalytic activity was evaluated by the

degradation of an RhB solution under visible light irradiation. For H_2O_2 alone, little photocatalytic degradation was observed, suggesting that H_2O_2 only participates in the redox action as a cocatalyst and has a minor influence on the final photocatalytic results. Hydroxyl radical produced by the photocatalytic decomposition of water plays a major role in the degradation of organic matter. In the process of photocatalytic degradation, sometimes a few drops of hydrogen peroxide can stimulate photocatalysis, which can improve the catalytic efficiency, because it is much easier to produce hydroxyl radicals by the degradation of hydrogen peroxide than water. The degradation ratio of bulk CN depicted in Fig. 10b was 46.9%/3 h. Furthermore, the photocatalytic kinetics followed a pseudo-first-order process[26], and the linear relationship between $\ln(c_0/c)$ and T is depicted in Fig. 10c and Fig. 10d. The rate constant of RhB photodegradation over CN was 0.003 58 min^{-1}. Etching treatment had a crucial influence on the photocatalytic activity of g-C_3N_4. After heat etching, the activity of the HCN sample was enhanced to 80.3%/3 h, possibly due to the morphology change of bulk g-C_3N_4. Although HCN has the same band structure as CN, heat etching significantly decreases the interlayer Van der Waals forces, efficiently exfoliates the bulk g-C_3N_4 and generates sheet-like g-C_3N_4. The increase in specific surface area can provide additional active sites and improve the photocatalytic performance. Acid etching not only increased the specific surface area but also decreased the band gap of g-C_3N_4, enabling the absorption of photons with longer wavelengths and thus a redshift in the optical absorption edge. However, the tri-s-triazine structure was damaged during the acid etching process, which led to defects in the recombination centers of photoexcited electron–hole pairs and led to a deterioration in catalytic activity. Therefore, the degradation ratio of ACN reached 81.3%/3 h, and the ACN rate constant was 2.8 times greater than that of CN. Coupling treatment with NH_4Cl significantly enhanced the photocatalytic performance of CN. At a content ratio of 5:4, the degradation ratio reached the highest value of 89.2%/3 h, and the rate constant was 3.4 times that of CN. It is notable that a further increase in NH_4Cl content led to a decrease in photocatalytic performance. Therefore, etching can change the band structure and the specific surface area. The CNN4 sample, which has features including good dispersion, lack of agglomeration and a 2D nanosheet structure, exhibited the greatest photocatalytic activity, which is attributed to two factors: 1) The narrow band gap can increase the wavelength range of absorbed photons and improve the concentration of photogenerated carriers; 2) The greater specific surface area offers more active absorption sites and photocatalytic reaction centers. To determine the ability of the g-C_3N_4 catalytic agent to degrade contaminants, RhB samples degraded by CNN4 for different degradation times were scanned by a UV-vis spectrometer, and the results are shown in Fig. 10e. As shown in the Fig. 10e, after 180 min of degradation, the color of the RhB solution gradually faded from purplish to colorless. The maximum absorption wavelength of the sample moves from 556 nm to 496 nm, and the intensity of the absorption peak decreases gradually. According to the research results, this process is in which RhB first gradually removed the ethyl group and then underwent ring-breaking mineralization. To further investigate the



(a) Photodegradation rate of systems with different NH_4Cl addition

(b) Photodegradation rate of systems with different treatment methods

(c) Pseudo-first-order reaction kinetics of systems with different NH_4Cl addition

(d) Pseudo-first-order reaction kinetics of systems with different treatment methods

(e) UV–vis spectra changes during RhB degradation by the CNN4 sample

(f) Degradation of tetracycline hydrochloride over the prepared samples

Fig. 10 Photodegradation properties of as-prepared samples

degradation range of the prepared samples, we further used tetracycline hydrochloride as the target to test the degrading ability of the CNN1-CNN5 samples. The results are shown in Fig. 10f. As shown in Fig. 10f, all five prepared samples showed some degree of degradation with the tetracycline hydrochloride solution. Among them, the CNN4 sample had the strongest degradation ability, and the degradation rate in 240 min was 83.2%. This result shows that the CNN4 sample has a strong photocatalytic degradation ability for tetracycline hydrochloride solution. The prepared samples can be used not only to degrade dye solution but also to degrade antibiotic solution.

It is well known that the process of photocatalytic degradation of organic pollutants is due to the photogenerated electrons (e^-) and holes (h^+) produced by the catalyst under the excitation of light. The formed e^- and h^+ react with the materials adsorbed on the surface of the catalyst to form superoxide radical ($\cdot O^{2-}$) and hydroxyl radical (·OH). Finally, these free radicals and h^+ react with organic pollutants to degrade and mineralize the pollutants. To investigate the role of free radicals and holes in the photocatalytic degradation of RhB by CNN4, p-benzoquinone (BQ) was selected as an ($\cdot O^{2-}$) free radical trapping agent, and ammonium oxalate (AO) was selected as a hole trapping agent. Isopropanol (IPA) was used as a trapping agent for ·OH free radicals. The test results are shown in Fig. 11. It can be seen from the diagram that after 3 h of photocatalytic degradation, the degradation rate of RhB by the CNN4 sample reached 89.2% without a trapping agent. After adding BQ, the degradation efficiency decreased significantly to 30%, while that of AO decreased to 60%. After adding IPA, the degradation efficiency was 90%. From the above data, it can be seen that $\cdot O^{2-}$ photogenerated holes play a major role in the photocatalytic reaction of RhB degradation by CNN4.

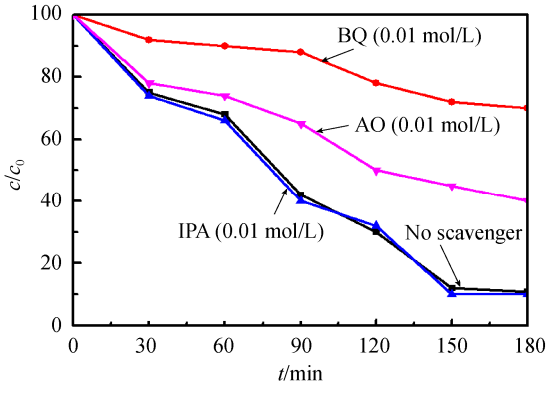


Fig. 11　Photocatalytic degradation of RhB over the CNN4 sample and with the addition of different scavengers

3.3　Photocatalytic mechanism of the 2D g-C_3N_4 nanosheets

Based on the above results, a tentative mechanism of the photocatalytic process is illustrated in Fig. 12 and is described by Eq. (7)–Eq. (12). Under visible light irradiation, electrons were excited from the VB to the CB of g-C_3N_4. The VB edge of g-C_3N_4 is not sufficiently positive to generate OH· or oxidize RhB. The CB is sufficiently more negative than $\cdot O_2$(–0.33 eV) to react with soluble oxides and generate $\cdot O_2$. H_2O_2 participates in the process as a cocatalyst. The presence of H_2O_2 not only produces OH· under light irradiation but also reacts with $\cdot O_2$ to generat e OH·. OH· is the second strongest oxidizing species after fluorine that can efficiently mineralize dye solution. The dominant radical reagents in the photocatalysis reaction are OH· and $\cdot O_2$. During the photocatalytic process, the concentrations of electrons and holes can be calculated by Eq. (13)–Eq. (15)[27].

$$\text{Semiconductor(SC)} \xrightarrow{h\nu} h^+_{(VB)} + e^-_{(CB)} \quad (7)$$

$$SC_{e^-_{(CB)}} + O_2 \rightarrow SC + \cdot O_2 \quad (8)$$

$$\cdot O_2 + \text{RhB} \rightarrow \text{Degradation product} \quad (9)$$

$$H_2O_2 \xrightarrow{h\nu} 2\text{OH}\cdot \quad (10)$$

$$O_2 + H_2O_2 \rightarrow \text{OH}\cdot + O_2 + \text{OH}^- \quad (11)$$

$$\text{OH}\cdot + \text{RhB} \rightarrow \text{Degradation products} \quad (12)$$

$$c_n c_p = N_- N_+ \exp[-E_g / kT] \quad (13)$$

$$N_- = \frac{2S_-(2\pi m^*_- k_B T)^{\frac{3}{2}}}{h^3} \quad (14)$$

$$N_+ = \frac{2S_+(2\pi m^*_+ k_B T)^{\frac{3}{2}}}{h^3} \quad (15)$$

where c_n and c_p are the concentrations of electrons and holes, respectively, and m is the mass of the electrons and holes. N_- is the effective state density of the conduction band and N_+ is the effective state density of the valence band. The concentrations of electrons and holes are constant under certain ambient conditions. The reaction between $\cdot O_2$ and H_2O_2 consumes the photoexcited electrons and generates extra electrons to produce more $\cdot O_2$, greatly improving the degradation rate E_{RhB}.

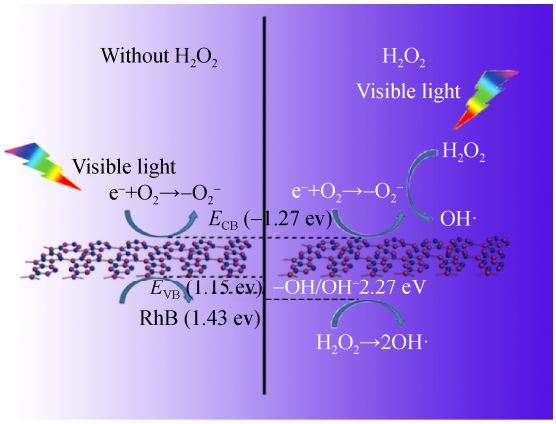


Fig. 12　Mechanism of photocatalytic activity

4 Conclusion

1) 2D nanosheet g-C_3N_4 was synthesized by thermal polycondensation and etching treatment, and the CNN4 sample exhibited a well-dispersed, agglomeration-free g-C_3N_4 material.

2) The crystal structure of the g-C_3N_4 samples did not change after etching. All three etching methods can effectively reduce the Van der Waals force between layers of g-C_3N_4. The CNN4 sample of g-C_3N_4 synergistically treated with NH_4Cl showed the best peeling effect, with a specific surface area of 22 m^2/g.

3) The CNN4 sample showed the best photocatalytic activity among all of the specimens with various NH_4Cl additions. During the degradation of RhB solution, the photocatalytic rates of CNN4, HCN and ACN were 3.4, 2.9 and 2.8 times higher than that of CN, respectively. In 240 min, the CNN4 sample degraded 83.2% tetracycline hydrochloride solution.

4) The dominant radical reagents in photocatalysis are $\cdot O_2$ and $OH\cdot$. H_2O_2 participated in the photocatalytic process as a cocatalyst. The probable mechanism of the photocatalysis reaction was investigated.

References:

[1] ZHANG H, LI X, FENG Z, et al. Effect of heating temperature on preparation of graphite-like g-C_3N_4 by pyrolysis of urea aqueous solution and its mechanism. J Chin Ceram Soc, 2017, 46(2): 281–287.

[2] GAO X, DAI H, ZHAO P, et al. Photocatalytic degradation on phenol of microwave-assisted synthesized graphitic carbon nitride. J Chin Ceram Soc, 2017, 45(10): 1503–1509.

[3] PAPAILIAS I, GIANNAKOPOULOU T, TODOROVA N, et al. Effect of processing temperature on structure and photocatalytic properties of g-C_3N_4 [J]. Appl Surf Sci, 2015, 358: 278–286.

[4] KISCH H. Semiconductor photocatalysis-mechanistic and synthetic aspects[J]. Angew Chem Int Ed, 2013, 52: 812–847.

[5] SU J, ZHU L, GENG P, et al. Self-assembly graphitic carbon nitride quantum dots anchored on TiO_2 nanotube arrays: An efficient heterojunction for pollutants degradation under solar light[J]. J Hazard Mater, 2016, 316: 159–168.

[6] LIU G, PAN J, YIN L, et al. Heteroatom-modulated switching of photocatalytic hydrogen and oxygen evolution preferences of anatase TiO_2 microspheres[J]. Adv Funct Mater, 2012, 22(15): 3233–3238.

[7] THOMPSON T L, YATES J T. Surface science studies of the photoactivation of TiO_2 new photochemical processes[J]. Chem Rev, 2006, (106): 4428–4453.

[8] FUJISHMA A, HONDA K. Electrochemical photolysis of water at a semiconductor electrode[J]. Nature, 1972, 238(5358): 37–38.

[9] SUN W T, YU Y, PAN H Y, et al. CdS quantum dots sensitized TiO_2 nanotube-array photoelectrodes[J]. J Am Chem Soc, 2008, 130: 1124–1125.

[10] MAMBA G, MISHRA A K. Graphitic carbon nitride (g-C_3N_4) nanocomposites: A new and exciting generation of visible light driven photocatalysts for environmental pollution remediation[J]. Appl Catal B: Environ., 2016, 198: 347–377.

[11] PARK H, KIM H, MOON G, et al. Photoinduced charge transfer processes in solar photocatalysis based on modified TiO_2[J]. Energy Environ Sci, 2016, 9: 411–433.

[12] WANG X, BLECHERT S, ANTONIETTI M. Polymeric graphitic carbon nitride for heterogeneous photocatalysis[J]. Acs Catal, 2012, 2(8): 1596–1606.

[13] LIU G, NIU P, SUN C, et al. Unique electronic structure induced high photoreactivity of sulfur-doped graphitic C_3N_4[J]. J Am Chem Soc, 2010, 132(33): 11642–11648.

[14] WANGY, WANG X, ANTONIETTI M. Polymeric graphitic carbon nitride as a heterogeneous organocatalyst: From photochemistry to multipurpose catalysis to sustainable chemistry[J]. Angew Chem Int Ed, 2012, 51(1): 68–89.

[15] ZHANG J, ZHANG M, LIN L, et al. Sol processing of conjugated carbon nitride powders for thin-film fabrication[J]. Angew Chem, 2015, 54(21): 6297–6301.

[16] MIAO H, ZHANG G, HU X, et al. A novel strategy to prepare 2D g-C_3N_4 nanosheets and their photoelectrochemical properties[J]. J Alloys Compd, 2017, 690: 669–676.

[17] WU M, YAN J M, ZHANG X W, et al. Synthesis of g-C_3N_4 with heating acetic acid treated melamine and its photocatalytic activity for hydrogen evolution[J]. Appl Surf Sci, 2015, 354: 196–200.

[18] YAN S C, LI Z S, ZOU Z G. Photodegradation performance of g-C_3N_4 fabricated by directly heating melamine[J]. Langmuir, 2009, 25 (17): 10397–10401.

[19] JIANG J, OU L Y, ZHU L, et al. Dependence of electronic structure of g-C_3N_4 on the layer number of its nanosheets: A study by Raman spectroscopy coupled with first-principles calculations[J]. Carbon, 2014, 80: 213–221.

[20] ZHANG J, ZHANG M, ZHANG G, et al. Synthesis of carbon nitride semiconductors in sulfur flux for water photoredox catalysis[J]. Acs Catal, 2012 , 2(6): 940–948.

[21] LU J, WANG Y, HUANG J, et al. One-step synthesis of g-C_3N_4 hierarchical porous structure nanosheets with dramatic ultraviolet light photocatalytic activity[J]. Mater Sci Eng B, 2016, 214: 19–25.

[22] ZHU B, ZHANG L, XU D, et al. Adsorption investigation of CO_2 on g-C_3N_4 surface by DFT calculation[J]. J CO_2 Util, 2017, 21: 327–335.

[23] SHI A, LI H, YIN S, et al. Effect of conjugation degree and delocalized π-system on the photocatalytic activity of single layer g-C_3N_4[J]. Appl Catal B: Environ, 2017, 218: 137–146.

[24] ZHU B, ZHANG J, JIANG C, et al. First principle investigation of halogen-doped monolayer g-C_3N_4 photocatalyst[J]. Appl Catal B: Environ, 2017, 207: 27–34.

[25] MA X, WEI Y, WEI Z, et al. Probing π-π stacking modulation of g-C_3N_4/graphene heterojunctions and corresponding role of graphene on photocatalytic activity[J]. J. Colloid Interface Sci, 2017, 508: 274–281.

[26] DENG Y, TANG L, ZENG G, et al. Insight into highly efficient simultaneous photocatalytic removal of Cr(VI) and 2,4-diclorophenol under visible light irradiation by phosphorus doped porous ultrathin g-C_3N_4 nanosheets from aqueous media: Performance and reaction mechanism[J]. Appl Catal B: Environ, 2017, 203: 343–354.

[27] VADIVEL S, MARUTHAMANI D, HABIB-YANGJEH A, et al. Facile synthesis of novel $CaFe_2O_4$/ g-C_3N_4 nanocomposites for degradation of methylene blue under visible-light irradiation[J]. J Colloid Interface Sci, 2016, 480: 126–136.